coatings

MDPI

Article

Thermal, Structural, Morphological and Electrical Characterization of Cerium-Containing 45S5 for Metal Implant Coatings

Sílvia Rodrigues Gavinho [1,*], Bruno Miguel Gonçalves Melo [1], João Paulo Borges [2], Jorge Carvalho Silva [3] and Manuel Pedro Fernandes Graça [1,*]

[1] I3N and Physics Department, Aveiro University, 3810-193 Aveiro, Portugal
[2] I3N-CENIMAT and Materials Science Department, NOVA School of Science and Technology, Campus de Caparica, 2829-516 Caparica, Portugal
[3] I3N-CENIMAT and Physics Department, NOVA School of Science and Technology, Campus de Caparica, 2829-516 Caparica, Portugal
* Correspondence: silviagavinho@ua.pt (S.R.G.); mpfg@ua.pt (M.P.F.G.)

Abstract: Biomaterial coatings on dental implants are increasingly being used as a solution to the problems of rejection and implant loss. Bioglass® has been seen as a promising material for coating metal implants, increasing the integration rate and improving the bond between the bone and the implant. Multifunctional bioactive glasses can exhibit antibacterial, antitumor and antioxidant effects with the addition of therapeutic ions. The cerium ion has shown an antioxidant effect through mimicking mechanisms and by acting as a scavenger of reactive oxygen species (ROS), which is important for avoiding oxidative stress post-surgery. Furthermore, it is possible to store electrical charge on the bioglass surface, which potentiates osseointegration. In this work, glasses with various percentages of cerium oxide (0.25, 0.5, 1 and 2 mol%) were developed and structurally and electrically analyzed. It was verified that the cerium insertion did not modify the amorphous phase characteristic of the glass but showed an increase in the number of non-bridging oxygens (NBOs). This increase in NBOs did not modify the electrical conductivity in either the ac or dc regime. The similar permittivity values of the glasses also suggest that their storage ability is unchanged with the addition of CeO_2. Concerning the impedance spectroscopy (IS) data, a decrease in resistance is visible with the addition of cerium oxide, suggesting a favorable behavior for applications as an antioxidant through the electro-Fenton reaction.

Keywords: Bioglass®; cerium; antioxidant effect; osteointegration; dielectric properties; implant coatings

Citation: Gavinho, S.R.; Melo, B.M.G.; Borges, J.P.; Silva, J.C.; Graça, M.P.F. Thermal, Structural, Morphological and Electrical Characterization of Cerium-Containing 45S5 for Metal Implant Coatings. *Coatings* **2023**, *13*, 294. https://doi.org/10.3390/coatings13020294

Academic Editor: Luka Pavić

Received: 22 December 2022
Revised: 19 January 2023
Accepted: 24 January 2023
Published: 28 January 2023

1. Introduction

Although titanium is widely used in the manufacturing of implants due to its biocompatibility and mechanical properties, it presents slow bone regeneration and instability during the healing phase. The consequences of this disadvantage can be reduced with surface treatments that allow the surface roughness to be increased, thus increasing the contact area at the implant–bone interface and consequently improving osseointegration.

However, this approach may not be enough for implant success due to the existence of failures related to inflammatory processes leading to loss of bone support and dental implants [1].

Coating implants with bioactive materials has been shown to provide a higher integration rate, promoting a faster and stronger bond between the bone and the implant. Bioactive glass coatings also prevent the corrosion and degradation of metallic implants and protect the surrounding environment from toxic products. Moreover, it is possible to introduce some therapeutic ions with several biological responses in the bioglass network, without significantly changing its structural properties [1–3].

In this way, researchers can combine the good mechanical properties of metallic implants with the bioactivity, biocompatibility and corrosion resistance of bioglass coatings [2].

Bioglass®, developed by Larry Hench in 1969, is one of the most studied glasses in the field of tissue regeneration and is composed of 46.1SiO_2-24.4Na_2O-26.9CaO-2.6P_2O_5 in mol%. This bioactive glass has been used as a coating for metal implants because it presents a higher bioactivity rate compared to other biomaterials due to its ability to form a carbonated layer of hydroxyapatite, very similar to the mineral phase composition of natural bone. The bond formed between the implant and the bone is so strong that it can only be removed by damaging the bone structure [4,5]. Furthermore, Bioglass® has osteoinductive and osteogenic properties due its ability to stimulate the recruitment of immature cells and their differentiation into osteoblasts, increasing their proliferation. Bioglass can also act as a matrix for the growth and development of bone cells and can promote the secretion of growth factors for the formation of new blood vessels, stimulating vascularization. The 45S5 glass composition also has antibacterial properties due to the rise in pH and osmotic pressure when in contact with a biological medium, but the most important feature is its biocompatibility.

Several therapeutic ions can be added to Bioglass® in order to promote specific biological responses. The cerium ion has presented several biological functions such as its antioxidant, bactericidal and bacteriostatic effects, role as an immunomodulator in degenerative pathologies and antitumor activity. The antioxidant effect of the cerium ion is due to its ability to exchange oxidation states between Ce^{3+} and Ce^{4+}, acting as a multienzyme mimic or a radical scavenger. One of its mimicking processes involves simulating the peroxidase activity capable of catalyzing peroxide reduction through a mechanism similar to the electro-Fenton reaction. This mechanism plays an important role in cellular metabolism by eliminating hydrogen peroxide, a reactive oxygen species (ROS), avoiding oxidative stress in the cells surrounding the implant after surgery and reducing the osseointegration time [6–11].

In addition, bioglass with CeO_2 does not exhibit cytotoxicity and increases osteoblast differentiation, mineralization of primary osteoblasts and collagen production [11]. Early osseointegration, enabled by various cerium-induced factors, also prevents bacterial adhesion and proliferation on the implant surface. The antibacterial effect of cerium oxide is also due to the interaction of cerium ions with bacteria, disrupting their wall and membrane and influencing their metabolic functions, such as respiration [12–18].

The storage of electrical charge on the surface of bioactive glass as a coating is promising and potentially revolutionary in the osteoconductivity and osseointegration capacity of metallic implants for dental and orthopedic applications. The nature (negative or positive charges) and amount of stored charge allow for the control of these biological properties. For bone tissue engineering applications, negatively charged surfaces have been shown to promote tissue formation and growth [19]. Bioglass® enables the storage of large quantities of electrical charges with a low polarization field due to the high mobility of the sodium ion chains and its glass composition [20]. Thus, it is important that the addition of cerium oxide does not compromise its performance with respect to electrical charge storage.

The main goals of this work are to analyze the potential of electrical charge stored in 45S5 with cerium ions and to verify if the addition of cerium is also promising for the antioxidant effect. For this purpose, impedance spectroscopy (IS) measurements were performed.

2. Materials and Methods

2.1. Synthesis Method

The base glass composition was synthesized considering Bioglass® developed by Hench et al. (46.1SiO_2-24.4Na_2O-26.9CaO-2.6P_2O_5, mol%), and 0.25, 0.5, 1 and 2 mol% of CeO_2 were added to the glass network [4]. The starting chemicals SiO_2, P_2O_5, $CaCO_3$, Na_2CO_3 and CeO_2 (Sigma-Aldrich) were mixed and homogenized, using a planetary ball milling process for 1 h at 300 rpm. The mixed powder was calcined for 8 h at 800 °C. The melt-quenching process was performed in a platinum crucible at 1300 °C for 1 h. The dif-

ferent compositions were re-melted with the same conditions to improve the homogeneity of the glasses. The molten bioglass was quenched by pouring it into a stainless-steel plate, at room temperature, and pressed by a second steel plate. Flat samples 1 mm in thickness with a diameter of 10 mm, approximately, were obtained. The base composition presented an un-colored and transparent glass. The presence of CeO_2 promotes a color change from light yellow to dark yellow.

2.2. Thermal Analysis

Differential thermal analysis (DTA) and thermogravimetric analysis (TG) were carried out on a Hitachi STA 7300 from room temperature up to 1200 °C with a heating rate of 5 °C/min. The measurements on powder samples obtained from the milling process were carried out under a 200 mL/min Nitrogen N50 (99.999%) atmosphere, and platinum crucibles were used.

2.3. Morphological and Structural Characterization

The X-ray diffraction (XRD) diffractograms of the samples, in powder form, were obtained at room temperature using an Aeris-Panalytical diffractometer, and CuKα radiation (λ = 1.54056 Å) was used, working at 40 kV and 15 mA. The scanning parameters were a scan step of 0.002°, and a 2θ angle range between 10° and 70°. Raman spectroscopy of the bulk samples was carried out using a Jobin Yvon HR800 spectrometer with an Ar+ laser (λ = 532 nm), and the spectra were obtained in a back-scattering geometry, between 200 and 1400 cm^{-1}.

The morphology of the bulk glasses was observed via scanning electron microscopy (SEM), performed using a Vega 3 TESCAN SEM microscope, on the free surface of the glasses. All samples were sputtered with carbon before the microscopic observation.

2.4. Electrical Characterization

In the electrical measurements, the bulk samples had a thickness of 1 mm. The surface area of all samples was measured with ImageJ software [21]. The opposite parallel faces of the samples were painted with silver conducting paste. The electrical measurements were performed using a nitrogen bath cryostat setup, in which the samples were maintained in a helium atmosphere to improve heat transfer and eliminate moisture. Both dc and ac measurements were assessed in the temperature range between 200 and 400 K. The dc conductivity was measured using a Keithley electrometer model 617A, applying 100 V, and after current stabilization, the measurement was registered. In the ac regime experiments, the dielectric spectroscopy measurements were accomplished using an impedance analyzer, Agilent 4294A, operating between 100 Hz and 1 MHz and measuring the impedance of the sample in the C_p-R_p configuration (the sample's capacitance in parallel with resistance). The real (ε') and imaginary (ε'') parts of the complex permittivity (ε^*) were calculated according to Equation (2) [22–25]:

$$\varepsilon^* = \varepsilon' - j\varepsilon'' = \frac{d}{A}\frac{C_p}{\varepsilon_0} - j\frac{d}{A}\frac{1}{\omega R_p \varepsilon_0} \quad (1)$$

where d represents the sample's thickness, A is the electrode area, ε_0 is the vacuum permittivity (8.8542×10^{-12} F/m) and ω is the angular frequency. The ac conductivity (σ_{ac}) was calculated using Equation (3) [26]:

$$\sigma_{ac} = \varepsilon'' \omega \varepsilon_0 \quad (2)$$

The temperature dependence of the electrical conductivity was adjusted using the Arrhenius model [27]:

$$\sigma = \sigma_0 exp\left(-\frac{E_a}{k_B T}\right) \quad (3)$$

where σ_0 is a pre-exponential factor, E_a is the activation energy, k_B is the Boltzmann constant and T is the temperature. E_a can be calculated from the slope of ln (σ) versus $1/T$.

In a second analysis, the complex impedance (Z^*) of the samples was measured in the frequency range from 0.01 Hz up to 1 MHz, using a Solartron Analytic Modulab Xm with a Linkam stage model HFS91, where the sample temperature was maintained stable at 37 °C.

3. Results and Discussion

Figure 1 shows the DTA-TG thermogram of the sample with 2% of CeO_2. The results suggest that the incorporation of CeO_2 in the glass network reduces the glass transition temperature (T_g = 545 °C) and crystallization temperature (T_c = 628 °C), compared with 45S5 (T_g = 552 °C, T_c = 728 °C), as verified in previous work [28]. This shift to lower temperatures can be associated with an increasing number of non-bridging oxygens (NBOs) in the glass network and a subsequent decrease in crystallization energy.

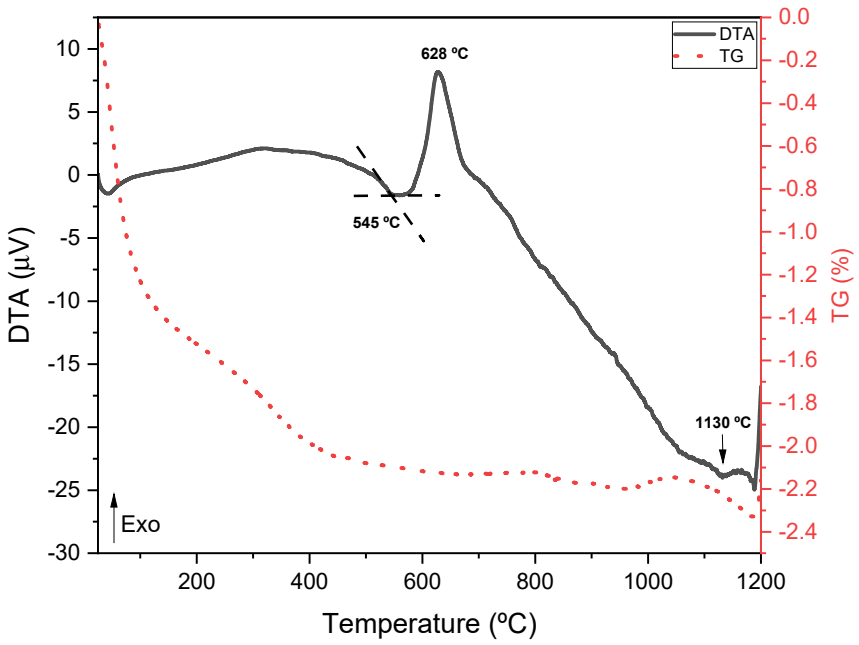

Figure 1. DTA-TG spectrum of the Ce2 sample at a heating rate of 5 °C/min.

To analyze the surface morphology of the bulk samples, scanning electron microscopy images were assessed (Figure 2). The 45S5 and Ce2 bulk samples show a characteristic morphology of glass without the presence of any crystalline phase.

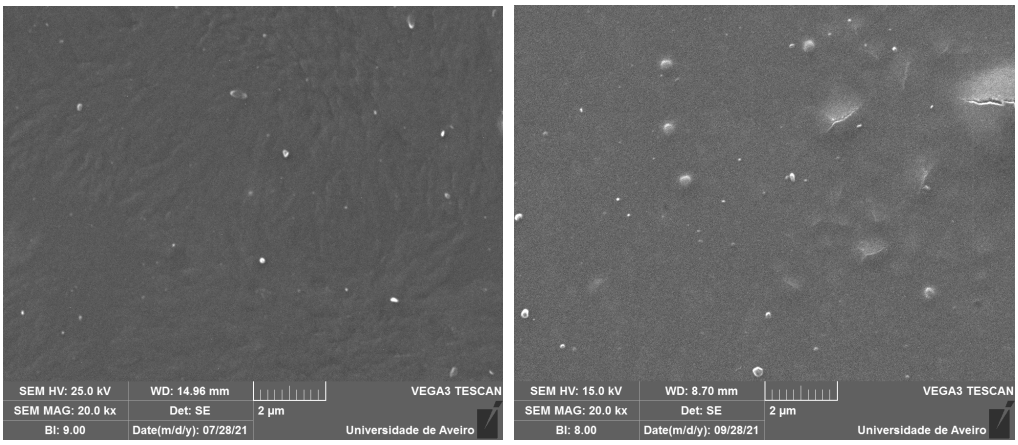

Figure 2. SEM micrographs of the 45S5 and Ce2 samples' surfaces (magnification: 20.0 kx).

The XRD results shown in Figure 3a present a broad band typical of an amorphous glass in the range of 25–38° for the 45S5 and Ce2 samples [29,30]. It is important to retain the network structure of Bioglass® because the dissolution of the bioglass and the kinetics of ion release are related to this property. Thus, the addition of CeO_2 will not compromise the bioactivity rate when in contact with the physiological medium [31]. Figure 3b presents the Raman spectra for all samples, showing a similar behavior between them. In agreement with the XRD patterns, the Raman results show the characteristic broad bands of the amorphous Bioglass® for all samples.

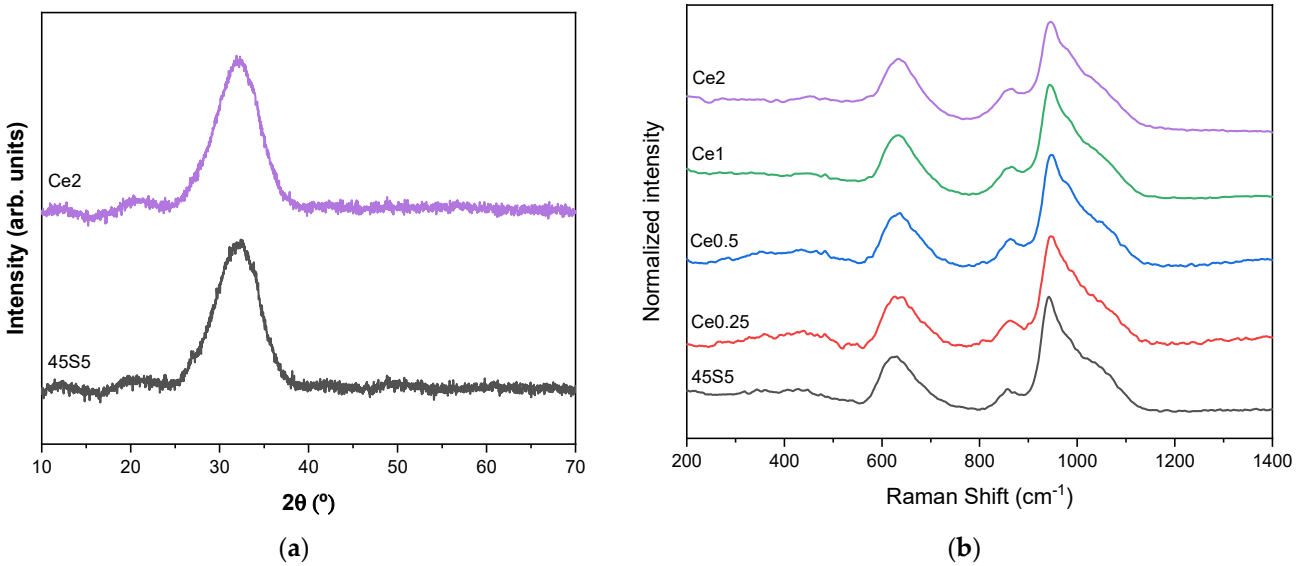

Figure 3. (**a**) XRD patterns of the 45S5 and Ce2 samples, and (**b**) Raman spectra of the 45S5, Ce0.25, Ce0.5, Ce1 and Ce2 samples.

The most interesting bands in silicate glass are the ones related to vibrations of asymmetric and symmetric stretching in the high-frequency region (800 and 1200 cm^{-1}). Figure 4 shows the Raman spectra deconvolution for the 45S5 sample and the 45S5 sample with 2% mol of CeO_2 in this region, revealing some differences in the band areas related to NBOs. Table 1 presents the specific analyses of the band areas for all Q units. The bands at 863–863 cm^{-1}, 903–911 cm^{-1}, 941 cm^{-1}, 966 cm^{-1}, 1004–1025 cm^{-1} and 1052–1068 cm^{-1} are related to Q_0 Si units, Q_1 Si units, Q_2 Si units, Q_0 P units, Q_1 P units and Q_3 Si units, respectively [32–35]. By analyzing Table 1, it can be seen that with the increase in the cerium concentration, the Q_0 Si units increase, creating more SiO_4 monomers, and the Q_0 P units decrease. In addition, in comparison to 45S5, except for Q_3, there is an increase in the NBO ions associated with Q_2 and Q_1, suggesting a transformation of Q_3 into units with more NBOs through the insertion of the network modifier.

Figure 5 shows the sum of all areas related to Q_0 units and Q_1, Q_2 and Q_3 units for all samples. The decrease in Q^0 units and the increase in Q_1, Q_2 and Q_3 Si units with the increase in cerium oxide are evident. The ratios between Q_0 and Q_1+Q_2+Q_3 in Ce0.25, Ce0.5 and Ce1 are similar, but in Ce2, the areas of Q_0 and Q_1+Q_2+Q_3 are the inverse of those of 45S5. The results suggest that the cerium ions promote the rise in NBO amounts, decreasing the monomer's Q_0 units.

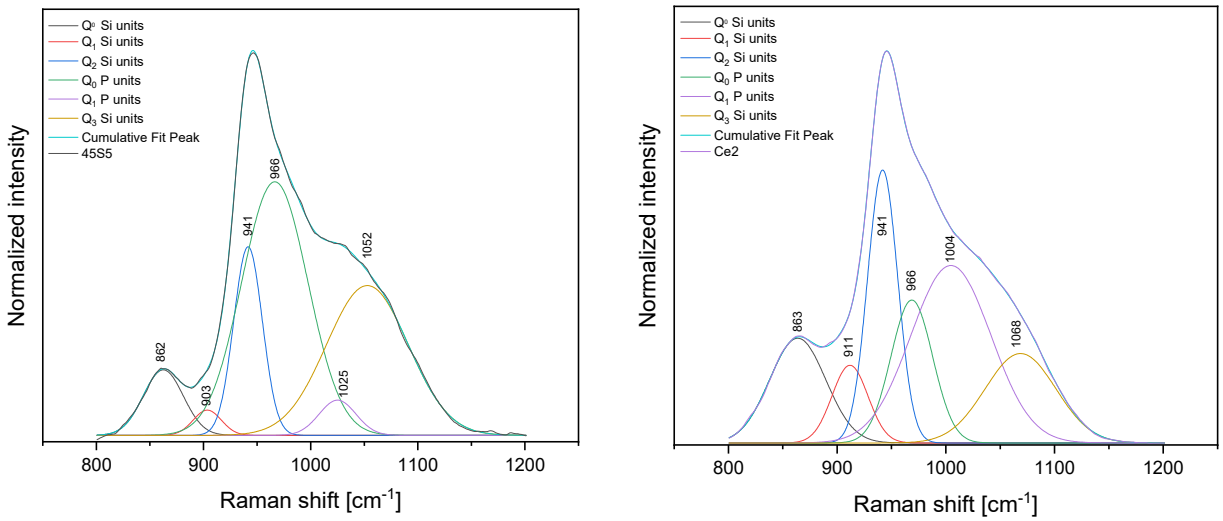

Figure 4. Deconvolution of Raman spectra for the (**a**) 45S5 and (**b**) Ce2 samples (R^2>0.999).

Table 1. Band areas of Q_0 Si units, Q1 Si units, Q_2 Si units, Q_0 P units, Q_1 P units and Q_3 Si units.

	Peak 1 Area (Q_0 Si Units)	**Peak 2 Area (Q_1 Si Units)**	**Peak 3 Area (Q_2 Si Units)**	**Peak 4 Area (Q_0 P Units)**	**Peak 5 Area (Q_1 P Units)**	**Peak 6 Area (Q_3 Si Units)**
45S5	7.8	2.13	15.9	49.9	3.9	36.7
Ce0.25	9.1	5.9	22.8	35.9	21	21.6
Ce0.5	11.1	5.7	26.6	34.3	16.8	24.3
Ce1	15.4	3.6	34	28.2	28.2	12.7
Ce2	16.9	8.1	23.8	17.4	41.1	18.3

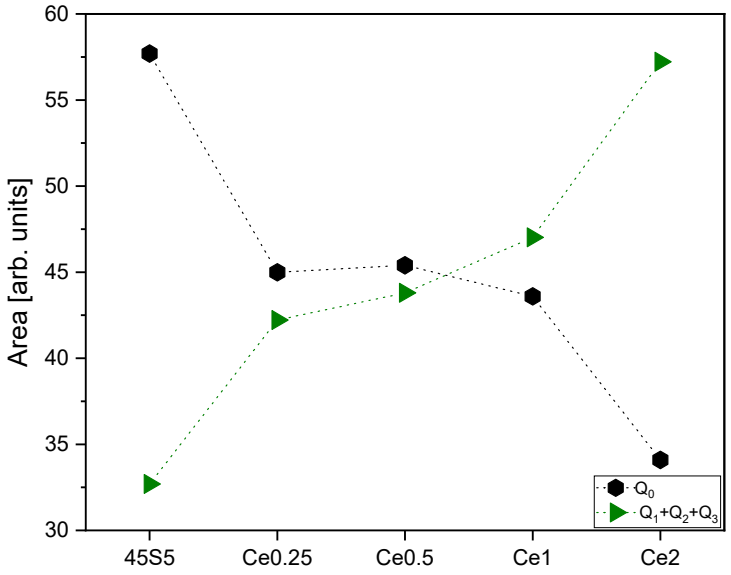

Figure 5. Sum of areas of Q_0 and Q_1+Q_2+Q_3 (NBOs) units of the 45S5, Ce0.25, Ce0.5, Ce1 and Ce2 samples.

Figure 6 shows the ac and dc conductivity behavior, as a function of temperature, for all samples. Analyzing the dc conductivity behavior, presented in Figure 6a, it is verified that for temperatures above 270 K, approximately, the logarithm of the conductivity becomes linear with the temperature, and therefore the Arrhenius equation can be applied to calculate the activation energy associated with this mechanism. In glasses, and at these

temperatures, the ionic contribution is higher than the electronic contribution. Thus, the ionic conductivity can be considered predominant in this temperature range and must be justified with the mobility of the Na ions, which, among all the network modifiers present in this glass composition (Na, Ca and Ce), are the ones with the lowest electronegativity value and atomic radius and therefore higher mobility [36–38]. For the ac conductivity, shown in Figure 6b at the fixed frequency of 10 kHz, the temperature profile is similar to that of the dc conductivity, suggesting that the responsible units are the same as those of the dc conductivity. As expected, the activation energy of the ac conductivity is lower than that calculated for the dc conductivity (Table 2). Moreover, there are no significant changes in the activation energy between samples. The same behavior is verified for the permittivity, which does not change significantly with the addition of CeO_2. This result shows that the insertion of cerium oxide, up to 2% mol, does not compromise the electrical charge storage characteristic of 45S5.

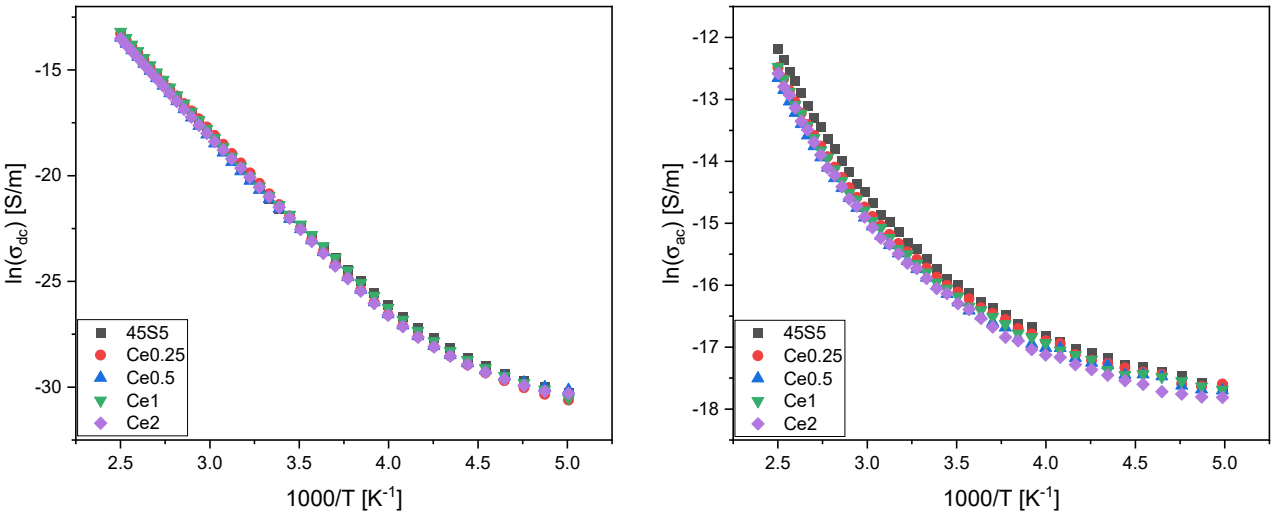

(**a**) (**b**)

Figure 6. The logarithm of conductivity versus 1000/T, for all samples in the (**a**) dc regime and (**b**) ac regime, at 10 kHz.

Table 2. Values of dc and ac conductivity and respective activation energies, and the permittivity at 10 kHz and 300 K.

	σ_{dc} (10^{-10}) [S/m]	$E_{a\,dc}$ [kJ/mol]	σ_{ac} (10^{-7}) [S/m]	$E_{a\,ac}$ [kJ/mol]	ε'	ε''
45S5	6.9 ± 0.1	77.7 ± 0.8	1.73 ± 0.02	40.99 ± 0.43	11.9 ± 0.7	0.31 ± 0.03
Ce0.25	8.7 ± 0.2	76.0 ± 0.8	1.48 ± 0.04	39.66 ± 0.41	11.7 ± 0.9	0.27 ± 0.04
Ce0.5	6.8 ± 0.1	78.9 ± 0.8	1.27 ± 0.02	39.62 ± 0.41	11.7 ± 0.6	0.23 ± 0.02
Ce1	7.9 ± 0.2	79.0 ± 0.8	1.38 ± 0.03	40.77 ± 0.42	12.0 ± 0.8	0.25 ±0.03
Ce2	7.6 ± 0.2	76.9 ± 0.8	1.26 ± 0.02	41.14 ± 0.43	12.0 ± 0.7	0.26 ± 0.02

In the Nyquist plot, it is verified that all samples present a dielectric relaxation that was adjusted to the equivalent circuit presented in Figure 7. For the equivalent circuit modeling, the impedance data were fitted using an application software developed by the authors in MATLAB [39]. This equivalent circuit is constituted by a resistor (R1) in parallel with a constant-phase element (CPE). The impedance of this element is given by the following equation:

$$Z^*_{CPE} = \frac{1}{A(j\omega)^n} \quad (4)$$

where A and n are frequency-independent parameters, but are usually temperature-dependent. The parameter n varies between 0 and 1. When n = 1, the CPE element reduces to a capacitive element, and when n < 1, it is possible to calculate the value of the real capacitance closest to the calculated CPE, through the following equation [40]:

$$C = Asin\left(\frac{n\pi}{2}\right)(\omega_{max})^{n-1} \quad (5)$$

where ω_{max} represents the frequency of the -Z″ maximum, associated with the observed relaxation phenomenon. At the temperature of 37 °C, a dielectric ratio phenomenon is observed in all the samples, which tend to shift towards lower values of Z′ and Z″ with the increase in the amount of cerium, as shown in Figure 7a. Figure 7b–d show the Nyquist plots for the 45S5, Ce0.5 and Ce2 samples, where a theoretical fit was performed based on the equivalent electric circuit presented in these figures. Figure 8a shows the variation in the imaginary part of the impedance with frequency for all samples. It is shown that the frequency at which the maximum occurs shifts to higher values with the increase in the number of cerium ions (Figure 8b), indicating a shorter relaxation time for the Ce2 sample and suggesting a greater mobility of the electric dipoles.

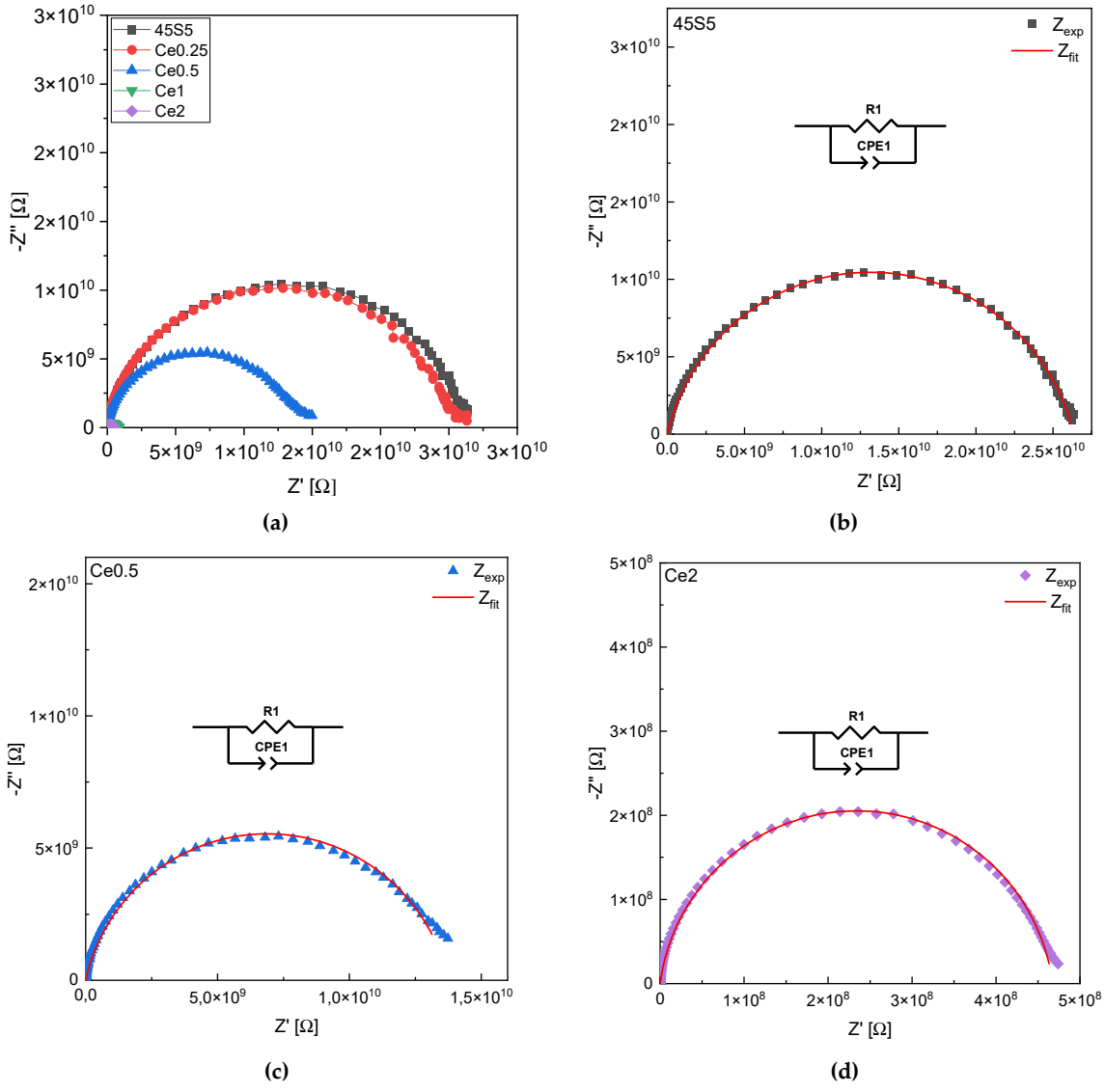

Figure 7. Z′ versus Z″, measured at 37 °C for (**a**) all samples (**b**) 45S5 sample (**c**) Ce0.5 sample and (**d**) Ce2 sample.

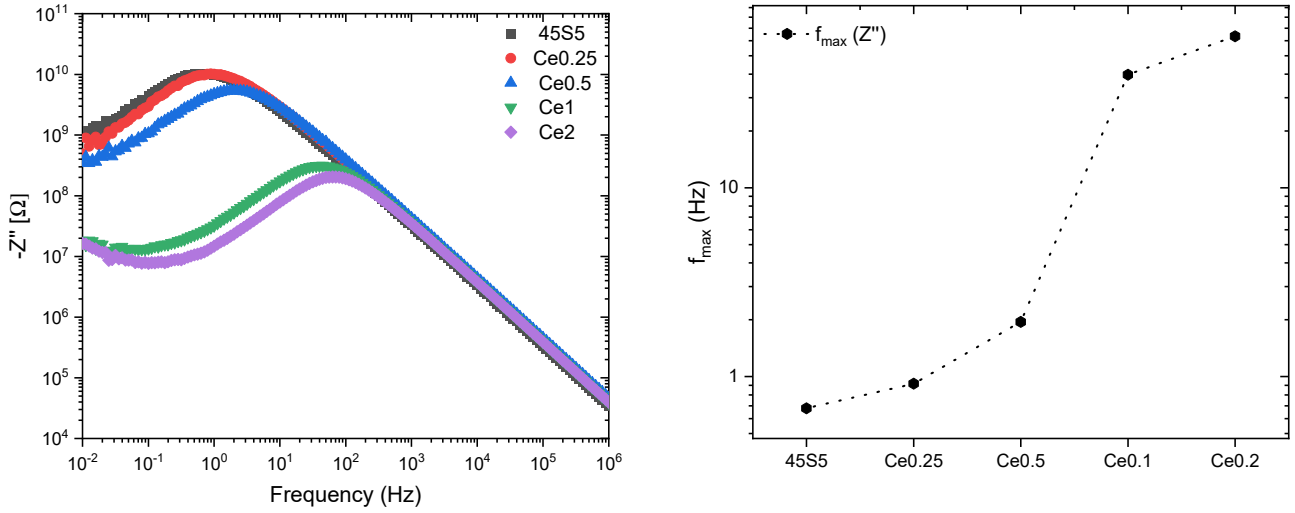

(**a**) (**b**)

Figure 8. (**a**) Z″ versus frequency at 37 °C; (**b**) frequency of the Z″ maximum as a function of the Ce content.

The R_1 resistance value decreases with the addition of CeO_2, and the same behavior is observed for the C parameter, as shown in Table 3. The resistance value can be related to the kinetics of the possible electro-Fenton reaction (EF) (Equations (6)–(8)). According to this information, the Ce2 sample should present an EF kinetic that is approximately 1.6, 29.5, 54.2 and 56.3 times higher than that of the samples with 1, 0.5, 0.25 and 0 mol% of cerium ions, respectively. This indicates that the increase in cerium enhances the EF reaction, with the Ce2 sample being the most promising to have an antioxidant effect [6,7].

$$Ce^{3+} + H_2O_2 + H^+ \rightarrow Ce^{4+} + OH\bullet + H_2O \quad (6)$$

$$OH\bullet + H_2O_2 \rightarrow HO_2^- + H_2O \quad (7)$$

$$Ce^{4+} + HO_2^- \rightarrow O_2 + Ce^{3+} + H^+ \quad (8)$$

Table 3. Electrical equivalent circuit fitting data.

	R_1 (10^8) [Ω]	A (10^{-11}) [$\Omega^{-1}s^n$]	n	C (10^{-12}) [F]
45S5	263	1.10	0.85	8.7
Ce0.25	253	0.86	0.87	6.7
Ce0.5	138	0.84	0.86	5.7
Ce1	7.3	0.92	0.91	5.5
Ce2	4.67	0.88	0.92	5.4

4. Conclusions

The insertion of CeO_2 does not modify the 45S5 glass network, retaining its amorphous structure and preserving its biological properties in terms of its reactivity/dissolution rate when in contact with the biological environment. The Raman results suggest a decrease in the amount of Q_0 units and an increase in Q_1, Q_2 and Q_3 numbers, related to NBOs, with the rise in cerium ions. The increase in the CeO_2 concentration does not decrease the potential to store electrical charge on the surface of 45S5. The dielectric response shows a decrease in resistance with increasing CeO_2, suggesting that the kinetics of the EF reaction in the 2% mol CeO_2 sample will be higher compared to the other samples.

All materials studied show potential as electrically charged coatings to increase the rate of bioactivity and improve the bond between the host bone and the implant, with the focus on the 45S5 sample with 2% mol of cerium oxide, as it also showed promising results in protecting cells from oxidative stress post-surgery.

Author Contributions: Conceptualization: S.R.G. and M.P.F.G.; methodology: S.R.G. and B.M.G.M.; software: S.R.G. and B.M.G.M.; investigation: S.R.G. and M.P.F.G.; writing—original draft preparation: S.R.G.; writing—review and editing: M.P.F.G., J.C.S. and J.P.B.; supervision: M.P.F.G. All authors have read and agreed to the published version of the manuscript.

Funding: This study was funded by FEDER funds through the COMPETE 2020 Program and National Funds through FCT—Portuguese Foundation for Science and Technology under the project LISBOA-01-0247-FEDER-039985/POCI-01-0247-FEDER-039985, LA/P/0037/2020, UIDP/50025/2020, and UIDB/50025/2020 of the Associate Laboratory Institute of Nanostructures, Nanomodelling, and Nanofabrication—i3N, UCIBIO (UIDP/04378/2020 and UIDB/04378/2020) and Associate Laboratory i4HB (LA/P/0140/2020). S.R. Gavinho acknowledges FCT—Portuguese Foundation for Science and Technology for the Ph.D. grant SFRH/BD/148233/2019. B.M.G. Melo acknowledges FCT—Portuguese Foundation for Science and Technology for the Ph.D. grant (SFRH/BD/117487/2016).

Institutional Review Board Statement: Not applicable.

Informed Consent Statement: Not applicable.

Data Availability Statement: Not applicable.

Acknowledgments: The authors extend their appreciation to the FEDER funds through the COMPETE 2020 Program and National Funds through FCT—Portuguese Foundation for Science and Technology under the project LISBOA-01-0247-FEDER-039985/POCI-01-0247-FEDER-039985, LA/P/0037/2020, UIDP/50025/2020, and UIDB/50025/2020 of the Associate Laboratory Institute of Nanostructures, Nanomodelling, and Nanofabrication—i3N., UCIBIO (UIDP/04378/2020 and UIDB/04378/2020) and Associate Laboratory i4HB (LA/P/0140/2020). S.R. Gavinho acknowledges FCT—Portuguese Foundation for Science and Technology for the Ph.D. grant SFRH/BD/148233/2019. B.M.G. Melo acknowledges FCT—Portuguese Foundation for Science and Technology for the Ph.D. grant (SFRH/BD/117487/2016).

Conflicts of Interest: The authors declare no conflict of interest.

References

1. Lung, C.Y.K.; Abdalla, M.M.; Chu, C.H.; Yin, I.; Got, S.R.; Matinlinna, J.P. A multi-element-doped porous bioactive glass coating for implant applications. *Materials* **2021**, *14*, 961. [CrossRef] [PubMed]
2. Sergi, R.; Bellucci, D.; Cannillo, V. A comprehensive review of bioactive glass coatings: State of the art, challenges and future perspectives. *Coatings* **2020**, *10*, 757. [CrossRef]
3. Iviglia, G.; Kargozar, S. Biomaterials, Current Strategies, and Novel Nano-Technological Approaches for Periodontal Regeneration. *J. Funct. Biomater.* **2019**, *10*, 3. [CrossRef]
4. Hench, L.L. The story of Bioglass®. *J. Mater. Sci. Mater. Med.* **2006**, *17*, 967–978. [CrossRef] [PubMed]
5. Joy-anne, N.O.; Su, Y.; Lu, X.; Kuo, P.H.; Du, J.; Zhu, D. Bioactive glass coatings on metallic implants for biomedical applications. *Bioact. Mater.* **2019**, *4*, 261–270. [CrossRef]
6. Kermani, F.; Vojdani-Saghir, A.; Mollazadeh Beidokhti, S.; Nazarnezhad, S.; Mollaei, Z.; Hamzehlou, S.; El-Fiqi, A.; Baino, F.; Kargozar, S. Iron (Fe)-doped mesoporous 45S5 bioactive glasses: Implications for cancer therapy. *Transl. Oncol.* **2022**, *20*, 101397. [CrossRef]
7. Xu, C.; Qu, X. Cerium oxide nanoparticle: A remarkably versatile rare earth nanomaterial for biological applications. *NPG Asia Mater.* **2014**, *6*, e90. [CrossRef]
8. Fan, M.; Liu, W.; Fan, C.; Zheng, X.; Hui, J.; Hu, C.; Fan, D. Ce and Se co-doped MBG/SA/HLC microgel bone powder for repairing tumor bone defects. *Nano Res.* **2022**, *16*, 746–756. [CrossRef]
9. Hammouda, H.F.; Farag, M.M.; El Deftar, M.M.F.; Abdel-Gabbar, M.; Mohamed, B.M. Ce-doped Nanobioactive Glass/Collagen/Chitosan Composite Scaffolds: Biocompatibility with Normal Rabbit's Osteoblast Cells and Anticancer Activity Test. *Adv. Anim. Vet. Sci.* **2022**, *10*, 712–724. [CrossRef]
10. Lord, M.S.; Berret, J.F.; Singh, S.; Vinu, A.; Karakoti, A.S. Redox Active Cerium Oxide Nanoparticles: Current Status and Burning Issues. *Small* **2021**, *17*, 2102342. [CrossRef]
11. Gavinho, S.R.; Pádua, A.S.; Sá-Nogueira, I.; Silva, J.C.; Borges, J.P.; Costa, L.C.; Graça, M.P.F. Biocompatibility, Bioactivity, and Antibacterial Behaviour of Cerium-Containing Bioglass®. *Nanomaterials* **2022**, *12*, 4479. [CrossRef] [PubMed]

12. Anesi, A.; Malavasi, G.; Chiarini, L.; Salvatori, R.; Lusvardi, G. Cell proliferation to evaluate preliminarily the presence of enduring self-regenerative antioxidant activity in cerium doped bioactive glasses. *Materials* **2020**, *13*, 2297. [CrossRef] [PubMed]
13. Malavasi, G.; Salvatori, R.; Zambon, A.; Lusvardi, G.; Rigamonti, L.; Chiarini, L.; Anesi, A. Cytocompatibility of potential bioactive cerium-doped glasses based on 45S5. *Materials* **2019**, *12*, 594. [CrossRef]
14. Raimondi, S.; Zambon, A.; Ranieri, R.; Fraulini, F.; Amaretti, A.; Rossi, M.; Lusvardi, G. Investigation on the antimicrobial properties of cerium-doped bioactive glasses. *J. Biomed. Mater. Res. Part A* **2021**, *110*, 504–508. [CrossRef]
15. Amaldoss, M.J.N.; Mehmood, R.; Yang, J.-L.; Koshy, P.; Kumar, N.; Unnikrishnan, A.; Sorrell, C.C. Anticancer therapeutic effect of cerium-based nanoparticles: Known and unknown molecular mechanisms. *Biomater. Sci.* **2022**, *10*, 3671–3694. [CrossRef] [PubMed]
16. Kurtuldu, F.; Mutlu, N.; Michálek, M.; Zheng, K.; Masar, M.; Liverani, L.; Chen, S.; Galusek, D.; Boccaccini, A.R. Cerium and gallium containing mesoporous bioactive glass nanoparticles for bone regeneration: Bioactivity, biocompatibility and antibacterial activity. *Mater. Sci. Eng. C* **2021**, *124*, 112050. [CrossRef]
17. Atkinson, I.; Anghel, E.M.; Petrescu, S.; Seciu, A.M.; Stefan, L.M.; Mocioiu, O.C.; Predoana, L.; Voicescu, M.; Somacescu, S.; Culita, D.; et al. Microporous and Mesoporous Materials Cerium-containing mesoporous bioactive glasses: Material characterization, in vitro bioactivity, biocompatibility and cytotoxicity evaluation. *Microporous Mesoporous Mater.* **2019**, *276*, 76–88. [CrossRef]
18. Qi, M.; Li, W.; Zheng, X.; Li, X.; Sun, Y.; Wang, Y.; Li, C.; Wang, L. Cerium and Its Oxidant-Based Nanomaterials for Antibacterial Applications: A State-of-the-Art Review. *Front. Mater.* **2020**, *7*, 213. [CrossRef]
19. Dubey, A.K.; Oyama, Y.; Kakimoto, K. Surface charge-assisted synthesis of ZnO on polarized $BaTiO_3$ substrate. *Ionics* **2019**, *25*, 1351–1358. [CrossRef]
20. Obata, A.; Nakamura, S.; Moriyoshi, Y.; Yamashita, K. Electrical polarization of bioactive glass and assessment of theirin vitro apatite deposition. *J. Biomed. Mater. Res.* **2003**, *67A*, 413–420. [CrossRef]
21. Schneider, C.A.; Rasband, W.S.; Eliceiri, K.W. Historical Commentary NIH Image to ImageJ: 25 years of image analysis. *Nat. Methods* **2012**, *9*, 671–675. [CrossRef]
22. Graça, M.P.F.; Ferreira da Silva, M.G.; Sombra, A.S.B.; Valente, M.A. The dielectric behavior of a thermoelectric treated B_2O_3-Li_2O-Nb_2O_5 glass. *J. Non-Cryst. Solids* **2008**, *354*, 3408–3413. [CrossRef]
23. Graça, M.P.F.; Ferreira da Silva, M.G.; Valente, M.A. Influence of thermal and thermoelectric treatments on structure and electric properties of B_2O_3-Li_2O-Nb_2O_5 glasses. *J. Non-Cryst. Solids* **2008**, *354*, 901–908. [CrossRef]
24. Graça, M.P.F.; Ferreira da Silva, M.G.; Sombra, A.S.B.; Valente, M.A. Electrical characterization of SiO_2:$LiNbO_3$ glass and glass-ceramics using dc conductivity, TSDC measurements and dielectric spectroscopy. *J. Non-Cryst. Solids* **2007**, *353*, 4390–4394. [CrossRef]
25. Jović, V.D. Calculation of a pure double layer capacitance from a constant phase element in the impedance measurements. *Zastita Materijala* **2022**, *63*, 50–57. [CrossRef]
26. Devaraja, C.; Gowda, G.V.J.; Eraiah, B.; Talwar, A.M.; Dahshan, A.; Nazrin, S.N. Structural, conductivity and dielectric properties of europium trioxide doped lead boro-tellurite glasses. *J. Alloys Compd.* **2022**, *898*, 162967. [CrossRef]
27. Javed, M.; Arif, A.; Kazmi, J.; Ambri, M.; Sha, M.; Iqbal, Y. Impedance spectroscopic study of charge transport and relaxation mechanism in $MnCr_2O_4$ ceramic chromite. *J. Alloy. Compd.* **2021**, *854*, 156996. [CrossRef]
28. Gavinho, S.R.; Graça, M.P.F.; Prezas, P.R.; Kumar, J.S.; Melo, B.M.G.; Sales, A.J.M.; Almeida, A.F.; Valente, M.A. Structural, thermal, morphological and dielectric investigations on 45S5 glass and glass-ceramics. *J. Non-Cryst. Solids* **2021**, *562*, 120780. [CrossRef]
29. Gavinho, S.R.; Prezas, P.R.; Graça, M.P.F. Synthesis, structural and electrical properties of the 45S5 Bioglass®. In *Electrical Measurements: Introduction, Concepts and Applications*; Nova Science Publishers Inc.: Hauppauge, NY, USA, 2017; pp. 295–320. ISBN 9781536129748.
30. Gavinho, S.R.; Prezas, P.R.; Ramos, D.J.; Sá-Nogueira, I.; Borges, J.P.; Lança, M.C.; Silva, J.C.; Henriques, C.M.R.; Pires, E.; Kumar, J.S.; et al. Nontoxic glasses: Preparation, structural, electrical and biological properties. *Int. J. Appl. Ceram. Technol.* **2019**, *16*, 1885–1894. [CrossRef]
31. Fernandes, H.R.; Gaddam, A.; Rebelo, A.; Brazete, D.; Stan, G.E.; Ferreira, J.M.F. Bioactive glasses and glass-ceramics for healthcare applications in bone regeneration and tissue engineering. *Materials* **2018**, *11*, 2530. [CrossRef]
32. Araujo, M.S.; Silva, A.C.; Bartolomé, J.F.; Mello-Castanho, S. Structural and thermal behavior of 45S5 Bioglass®-based compositions containing alumina and strontium. *J. Am. Ceram. Soc.* **2020**, *103*, 3620–3630. [CrossRef]
33. Dziadek, M.; Zagrajczuk, B.; Jelen, P.; Olejniczak, Z.; Cholewa-Kowalska, K. Structural variations of bioactive glasses obtained by different synthesis routes. *Ceram. Int.* **2016**, *42*, 14700–14709. [CrossRef]
34. Berezicka, A.; Szumera, M.; Sułowska, J.; Jeleń, P.; Olejniczak, Z.; Stępień, J.; Zając, M.; Pollastri, S.; Olivi, L. Unraveling the nature of sulfur-bearing silicate-phosphate glasses: Insights from multi-spectroscopic (Raman, MIR, ^{29}Si, ^{31}P MAS-NMR, XAS, XANES) investigation. *Ceram. Int.* **2022**, *48*, 4238–4254. [CrossRef]
35. Sun, Y.; Zhang, Z.; Liu, L.; Wang, X. FTIR, Raman and NMR investigation of CaO-SiO_2-P_2O_5 and CaO-SiO_2-TiO_2-P_2O_5 glasses. *J. Non-Cryst. Solids* **2015**, *420*, 26–33. [CrossRef]
36. Graça, M.P.F.; Ferreira da Silva, M.G.; Valente, M.A. $NaNbO_3$ crystals dispersed in a B_2O_3 glass matrix—Structural characteristics versus electrical and dielectrical properties. *Solid State Sci.* **2009**, *11*, 570–577. [CrossRef]
37. Graça, M.P.F.; Ferreira da Silva, M.G.; Sombra, A.S.B.; Valente, M.A. Electric and dielectric properties of a SiO_2-Na_2O-Nb_2O_5 glass subject to a controlled heat-treatment process. *Phys. B Condens. Matter* **2007**, *396*, 62–69. [CrossRef]

38. Keshri, S.R.; Ganisetti, S.; Kumar, R.; Gaddam, A.; Illath, K.; Ajithkumar, T.G.; Balaji, S.; Annapurna, K.; Nasani, N.; Krishnan, N.M.A.; et al. Ionic Conductivity of $Na_3Al_2P_3O_{12}$ Glass Electrolytes—Role of Charge Compensators. *Inorg. Chem.* **2021**, *60*, 12893–12905. [CrossRef]
39. Melo, B.M.G.; Loureiro, F.J.A.; Fagg, D.P.; Costa, L.C.; Graça, M.P.F. DFRTtoEIS: An easy approach to verify the consistency of a DFRT generated from an impedance spectrum. *Electrochim. Acta* **2021**, *366*, 137429. [CrossRef]
40. Jovic, V.D.; Jovic, B.M. EIS and differential capacitance measurements onto single crystal faces in different solutions: Part I: Ag(111) in 0.01 M NaCl. *J. Electroanal. Chem.* **2003**, *541*, 1–11. [CrossRef]